

Functional Tomographic Fluorescence Imaging of pH Microenvironments in Microbial Biofilms by Use of Silica Nanoparticle Sensors^{∇†}

Gabriela Hidalgo,^{1‡} Andrew Burns,^{2‡} Erik Herz,² Anthony G. Hay,³ Paul L. Houston,⁴ Ulrich Wiesner,^{2*} and Leonard W. Lion^{1*}

School of Civil and Environmental Engineering, Hollister Hall, Cornell University, Ithaca, New York 14853¹; Department of Materials Science and Engineering, 214 Bard Hall, Cornell University, Ithaca, New York 14853²; Department of Microbiology, B35A Wing Hall, Cornell University, Ithaca, New York 14853³; and School of Chemistry and Biochemistry, Administration Building, Georgia Institute of Technology, Atlanta, Georgia 30332⁴

Received 28 May 2009/Accepted 27 September 2009

Attached bacterial communities can generate three-dimensional (3D) physicochemical gradients that create microenvironments where local conditions are substantially different from those in the surrounding solution. Given their ubiquity in nature and their impacts on issues ranging from water quality to human health, better tools for understanding biofilms and the gradients they create are needed. Here we demonstrate the use of functional tomographic imaging via confocal fluorescence microscopy of ratiometric core-shell silica nanoparticle sensors (C dot sensors) to study the morphology and temporal evolution of pH microenvironments in axenic *Escherichia coli* PHL628 and mixed-culture wastewater biofilms. Testing of 70-, 30-, and 10-nm-diameter sensor particles reveals a critical size for homogeneous biofilm staining, with only the 10-nm-diameter particles capable of successfully generating high-resolution maps of biofilm pH and distinct local heterogeneities. Our measurements revealed pH values that ranged from 5 to >7, confirming the heterogeneity of the pH profiles within these biofilms. pH was also analyzed following glucose addition to both suspended and attached cultures. In both cases, the pH became more acidic, likely due to glucose metabolism causing the release of tricarboxylic acid cycle acids and CO₂. These studies demonstrate that the combination of 3D functional fluorescence imaging with well-designed nanoparticle sensors provides a powerful tool for in situ characterization of chemical microenvironments in complex biofilms.

Biofilms are collections of surface-attached microbes entrapped in a self-produced matrix of extracellular polymeric substances anchored to a surface (17). Their growth is characterized by complex three-dimensional (3D) structures including channels, voids, towers, and mushroom-like protrusions (9). They are common both in biological systems and in near-surface fluid rock systems and may occupy a significant portion of the surface area exposed to fluids in many natural environments, including fresh and saline surface waters, ground waters, deep-sea hydrothermal systems, and deep sedimentary basins (41, 51). The ubiquity of biofilms has a variety of important implications for modern society. Industrially, biofilms are used in a wide array of engineered systems, including treatment of wastewater and hazardous waste, contaminated soils, and oil spills (43). Conversely, biofilms can also contaminate water distribution systems, foul the hulls of ships, and promote corrosion (30). Medically, biofilms have been impli-

cated in lung and chronic wound infections, as well as in catheter and implant colonization, in cystic fibrosis, in tuberculosis, in dental caries, and in periodontal diseases (12, 17).

One prominent characteristic of biofilms is the development of 3D chemical gradients from the diffusion of nutrients, metabolic products, and signaling molecules throughout the film. These gradients create microenvironments in which the local physicochemical properties may differ substantially from those in the surrounding solution (48). This gradation of conditions allows, for example, anaerobic bacteria to flourish within biofilms that are growing in an otherwise aerobic environment (23, 36). Another example of the effects of biofilm-generated chemical gradients is dental caries. Following sugar consumption, the pH within a dental plaque biofilm drops dramatically (<5.5) while the pH of the overlying saliva remains near neutral. This acidification leads to demineralization of the tooth enamel and ultimately caries (33, 34).

Several techniques have been used to analyze pH gradients in biofilms, and each has its own benefits and limitations. Most recently, Beveridge and Hunter (22) used seminaaphthorhodafuor-4F 5 (and 6)-carboxylic acid (C-SNARF-4), a ratiometric fluorescent dye, to measure pH microenvironments in *Pseudomonas aeruginosa* biofilms and observed pH values that ranged from 5.6 to 7.0. This method minimizes perturbations of the biofilm, and its spatial resolution is limited only by that of the microscope in use. Unfortunately, free sensor dyes have been demonstrated to interact with biofilm components, potentially altering their sensitivities and perturbing the result-

* Corresponding author. Mailing address for Ulrich Wiesner: Department of Materials Science & Engineering, Cornell University, 214 Bard Hall, Ithaca, NY 14853. Phone: (607) 255-3487. Fax: (607) 255-2365. E-mail: ubw1@cornell.edu. Mailing address for Leonard W. Lion: School of Civil and Environmental Engineering, Cornell University, Hollister Hall, Ithaca, NY 14853. Phone: (607) 255-7571. Fax: (607) 255-9004. E-mail: LWL3@cornell.edu.

‡ These authors contributed equally to this work.

† Supplemental material for this article may be found at <http://aem.asm.org/>.

[∇] Published ahead of print on 2 October 2009.

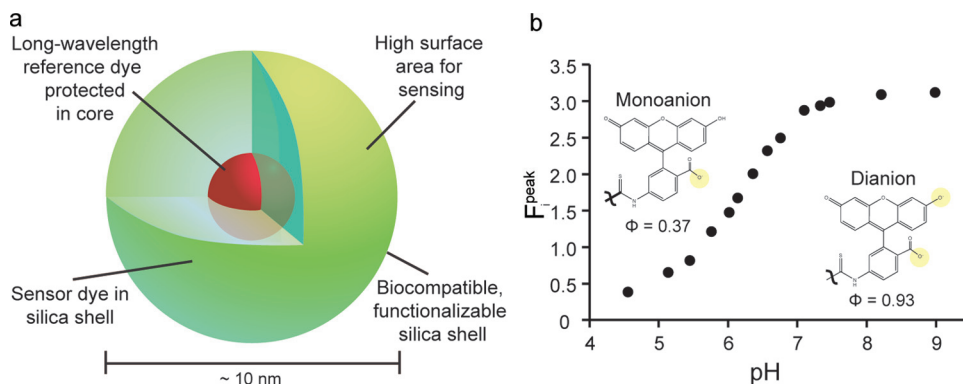


FIG. 1. Sensor schematic and calibration. (a) Schematic diagram showing the core-shell architecture of a C dot sensor that highlights the reference dye (Cy5) sequestered in the core and coated by a sensor dye (fluorescein) shell. (b) Peak fluorescein emission collected for solutions of known pH values ranging from 4.5 to 9.0. Also shown is the molecular structure of the dye in its dianionic charge state, where it exhibits a quantum yield of approximately 93%, and in its monoanionic state, where its quantum yield is approximately 37%.

ing images (22). Further, the penetration of any molecular or nanometer-size probe into the biofilm can be limited by the decreased diffusion rates within the dense microcolony environment (55). Finally, as with all free dye molecules, brightness and photostability are limited and photoexcitation can cause cellular toxicity (4). Microelectrode-based techniques have also been used on a large variety of biological systems (27, 42, 49), but the spatial resolution of microelectrode-based techniques is limited by the tip size and insertion of the microelectrode into the biofilm inherently perturbs the local surroundings. Each data point obtained with a microsensors is a single measurement integrated over a spatial volume covering approximately twice the tip diameter (14), which limits the ultimate spatial resolution of the sensor. In addition, a systematic study of a common microelectrode system revealed highly variable accuracy and precision between different electrodes (29).

Finally, fluorescence lifetime imaging can be used to measure chemical concentrations through the use of appropriate dye molecules. By imaging a sample with a pulsed laser and analyzing the decay rate of the dyes in the sample as they fluoresce, Vroom et al. (55) were able to measure pH in a mixed culture of oral bacteria. One hour after the biofilms were exposed to 14 mM sucrose, pH was measured throughout the biofilm and values ranged from 7.0 to 5.5 were observed. This technique provides great definition and tissue penetration; however, the equipment needed to perform fluorescence lifetime imaging includes fast detectors and electronics capable of differentiating nanosecond emissions in addition to a pulsed laser excitation source and is not universally available. Detailed reviews of this method may be found elsewhere (2, 6).

We implemented 3D (tomographic) fluorescence imaging with ratiometric silica nanoparticle sensors to study the morphology and temporal evolution of pH microenvironments in *Escherichia coli* PHL628 and mixed-culture wastewater biofilms. Because of the diversity of structure and environments, functional tomographic imaging is of particular interest for investigating biofilms in their native state. Tomographic imaging techniques such as optical coherence tomography (58), soft X-ray microscopy (25), and confocal fluorescence microscopy (38) enable high-resolution structural reconstructions with minimal perturbation of the biofilm. We have chosen the spa-

tial variation of pH within microbial biofilms to test tomographic imaging via confocal fluorescence microscopy as it is an exciting area of research relevant to both the industrial and clinical impacts of biofilms. From a clinical standpoint, non-uniform pH profiles in biofilm infections are important because the degree of physiological heterogeneity, marked by the establishment of nutrient, dissolved gas, and pH gradients increases with time and is positively correlated with the development of drug resistance (15). Furthermore, it has been well established that the susceptibility of bacterial cells to antibiotics and biocides is profoundly affected by their pH, among other factors (15). The recent emergence of antibiotic-resistant pathogenic bacteria makes this a topic of great interest (11, 15, 17).

We employed ratiometric core-shell silica nanoparticle sensors, referred to as C dot sensors (5), in order to overcome the limitations of free ratiometric sensor dyes. As shown schematically in Fig. 1a, incorporating green-emitting, pH-sensitive dye molecules (fluorescein) in a thin silica shell surrounding a core rich in red-emitting, pH-insensitive dye molecules (Cy5) (5) permits ratiometric quantification of the local pH by comparison of sensor and reference dye emission intensities (Fig. 1b). This internally standardized design allows the analyte concentration to be measured independently of changes in the sensor concentration, unlike single-color sensor imaging, which can only give a qualitative description of the local environment (8, 16, 26). Further, the covalent incorporation of dyes into a core-shell silica matrix significantly enhances both dye brightness and photostability through increases in the radiative fluorescence rate and decreases in the nonradiative fluorescence rate (31). Finally, silica is a highly biocompatible and easily functionalized material for diverse biological applications (4, 7). As is demonstrated below, however, only if the C dot sensors are kept below a critical particle size is homogeneous biofilm staining possible. This discovery enabled, to the best of our knowledge, the first functional volumetric imaging of pH in prokaryotic systems using ratiometric nanoparticle sensors.

MATERIALS AND METHODS

C dot sensors. C dot sensors with 70-, 30-, and 10-nm diameters were grown via modified Stöber silica nanoparticle syntheses (31, 50). Amination was per-

formed by using 3-aminopropyl triethoxysilane as a surface-silanzing agent. The 10-nm-diameter bare silica particles which were ultimately used for all of the functional 3D reconstructions shown here consist of a particle core covalently incorporating Cy5 as an environmentally insensitive reference dye via coupling to a reactive silane, surrounded by a shell covalently incorporating fluorescein dye (fluorescein isothiocyanate [FITC]) through coupling to a reactive silane. FITC was chosen for its pK_a of 6.4, which is within the range of interest for this biological system. At $pH \geq 9$, FITC exists in the dianionic charge state and exhibits a quantum yield of approximately 93%, while at $pH \leq 4.5$, the dye is protonated to the monoanionic state with a quantum yield of approximately 37% (Fig. 1b) (18). Cy5 has a quantum yield that is constant within this pH range, making it an ideal internal standard. Additional information on the synthesis and characteristics of these particles may be found elsewhere (4, 5, 31).

Culture and media. *E. coli* PHL628, an adherent K-12 MG1655 derivative, was used as the test bacterium for the pure-culture experiments. This strain has a mutation in the *ompR* gene that results in overproduction of curli, thin fibrillar pili at the surface of the cells that allow the bacteria to adhere and form sessile communities (54). The cultures were grown in a solution of 1 part Luria-Bertani (LB) medium (which contained, per liter, 10 g NaCl, 10 g tryptone, and 5 g yeast extract) and 2 parts water and which was sterilized by autoclaving at 121°C before use. All experiments performed with *E. coli* PHL628 were supplemented with kanamycin (50 mg/liter). Suspended cultures were grown at 37°C with rotary shaking at 150 rpm. Attached cultures were grown in 35-mm petri dishes with an untreated 14-mm Microwell no. 1.5 coverglass at the bottom surface (MatTek, Ashland, MA). After inoculation, the cells were kept at 30°C with rotary shaking at 30 rpm. Every 48 h, the medium was discarded and fresh medium was added. Biofilms were grown for 7 to 8 days. Approximately 9 h prior to imaging, the C dot sensors were added (to a concentration of 50 nM) and the cultures were continuously stirred for 4 h. Approximately 5 h prior to imaging, the biofilms were washed twice to remove unbound dots and fresh medium was added.

The mixed-culture seed (potentially containing archaeal and eukaryotic microorganisms, e.g., fungi and protozoans, in addition to bacteria) (24) came from a municipal wastewater treatment facility in Ithaca, NY. Biofilms and suspended mixed cultures were grown by following the protocols described above.

Growth curves. To investigate the biocompatibility and potential toxicity of the core-shell silica nanoparticles, 10-nm-diameter sensor particles and dye-free nanoparticles of the same size were added to diluted LB medium at various concentrations representative of biofilm growth conditions (18 to 50 nM). The solutions were then inoculated at 1% volume with either *E. coli* PHL628 cultures or mixed wastewater cultures. Culture aliquots of 200 μ l were placed in sterile, clear 96-well plates, and optical density (OD) at 600 nm was recorded until stationary phase was reached. OD was measured with a Biotek multidetection microplate reader equipped with Synergy HT and KC4 software. The microplate reader maintained the cultures at 37°C with shaking prior to each measurement, and measurements were performed at 20-min intervals. Each condition was analyzed in triplicate. Sterile controls both with and without particles were also analyzed. Reported ODs correspond to the absorbance measured at the bottom of each well through approximately 3 mm of medium; therefore, our OD values are not comparable to standard OD measurements with cuvettes with a 1-cm path length.

pH analysis in suspended cultures. A calibration curve for C dot sensors was generated by mixing the dots with a series of pH-adjusted phosphate-buffered saline solutions (pH 4.0 to 8.0) and measuring sensor (green) and reference (red) emission spectra upon excitation at 488 and 633 nm, respectively, on a PTI spectrofluorometer (see Fig. S3a and b in the supplemental material, respectively). For each measurement, the peak intensity ratio ($F_i = I_{FITC}/I_{Cy5}$; see Fig. S3c in the supplemental material) was plotted versus pH and analyzed by using the equation $pH = pK_a + \log[(F_i - F_{min})/(F_{max} - F_i)]$, a modified Henderson-Hasselbalch equation where F_{min} and F_{max} are the extreme values of F_i at low and high pHs, respectively, to determine the pK_a and generate a calibration curve (see Fig. S3d in the supplemental material).

One-hundred-milliliter volumes of overnight cultures of *E. coli* PHL628 grown in 1/3 LB medium were spiked with a concentrated glucose solution to achieve a final concentration of 90 mM glucose or an equal volume of distilled water (control). For the following 12 h, 700- μ l aliquots were retrieved from the spiked flask, as well as the 0 mM glucose control, and placed in cuvettes, where the suspensions were mixed with C dots to a concentration of 180 nM. Fluorescence in the green and red channels was recorded at the excitation and emission wavelengths described above. pH was simultaneously recorded with a UP-10 Denver Instrument pH meter. The experiment was simultaneously performed with the mixed wastewater culture. Next, the relationship obtained from the calibration curve ($r^2 = 0.99$) was used to calculate the pH of the cell suspensions.

Imaging. All biofilm images were collected with a Leica TCS-SP2 confocal laser scanning microscope equipped with argon ion and helium-neon lasers. A 40 \times 0.8 numerical aperture water immersion objective was used for all imaging. TIF images of 512 by 512 pixels were collected at 12-bit color depth in *xy* mode. Image stacks were generated by sequential imaging in 1- μ m steps through the biofilm.

To determine the spatial distribution of pH microenvironments within the biofilms, both *E. coli* PHL628 and mixed-culture films were grown and mixed with the sensors as described above. The samples were maintained at room temperature and under constant shaking at 30 rpm until imaging. The biofilms were concurrently imaged by using transmitted light and fluorescence with excitation at 488 and 633 nm and appropriate emission filter settings. Particle-free biofilms were similarly imaged to control for background fluorescence. In order to record pH variations in biofilms following a glucose spike, an initial series of images was taken as a baseline, followed by a glucose addition that resulted in a final concentration equal to that used for the suspended cultures (90 mM). The same field was imaged every 30 min for the next 1.5 h. For calibration, aliquots of phosphate-buffered saline solutions were mixed with particles to a final concentration of 15 μ M and imaged in 96-well plates.

Image analysis. Analysis routine examples are included in the supplemental material as MATLAB code. Briefly, all image files were loaded into MATLAB 7.4.0 by using the *imread* command and background corrected based on average background images taken at each image setting. For the calibrations, replicates in each channel, at each pH, were median filtered (to remove noise) and averaged prior to pixelwise division of the green (sensor) channel by the red (reference) channel to determine $F_i(I_{FITC}/I_{Cy5})$. The mean and standard deviation of this ratio were calculated across each image and used as the F_i values in the modified Henderson-Hasselbalch equation described in Materials and Methods.

For the biofilm images, each sensor and reference channel image was divided pixelwise to generate F_i values throughout the imaging field and the pH was calculated at each point which contained sufficient reference intensity to be considered above the background. The 512-by-512 arrays of pH values were scaled for output as 8-bit grayscale TIFs from MATLAB in the order in which they were read, and a pH scale bar was appended. The images were then imported into the Osirix DICOM image processing software (44). Originally designed for magnetic resonance imaging, computed tomography, and position emission tomography image analysis, the software creates 3D tomographs from 2D image stacks in a variety of false-spectrum colors and allows manipulation of the data and export to still images (see Fig. 3 to 6), as well as video (see the supplemental material).

RESULTS

C dot sensor distribution and toxicity. We assayed biofilms with C dot sensors of various diameters (70, 30, and 10 nm) and both positively charged (aminated) and negatively charged (bare silica) surfaces. The amination process screened the local pH effects on the particle, making sensing difficult, and thus was not pursued further.

For 70- and 30-nm-diameter bare silica sensors, the particles were distributed sparsely and heterogeneously in the biofilms and a majority of the beads were removed during the washing steps. Furthermore, upon imaging, the biofilm did not overlie the C dots; rather, those dots that remained agglomerated in clusters separate from the bacteria (data not shown). Only when using the smallest, 10-nm-diameter bare C dot sensors were we able to reproducibly achieve high and homogeneous biofilm incorporation. The following experiments were all performed with the bare 10-nm particles.

Measurements to determine the kinetics of the integration of the particles into the matrix were not performed. The dots were assumed to be able to diffuse into the biofilm and anchor to cells or extracellular polysaccharide in the 4 h provided between the C dot sensor addition and the washing that eliminated unbound dots. It is reasonable to assume that an active equilibrium was reached within this period of time and that some of the particles may have been detaching and reattaching

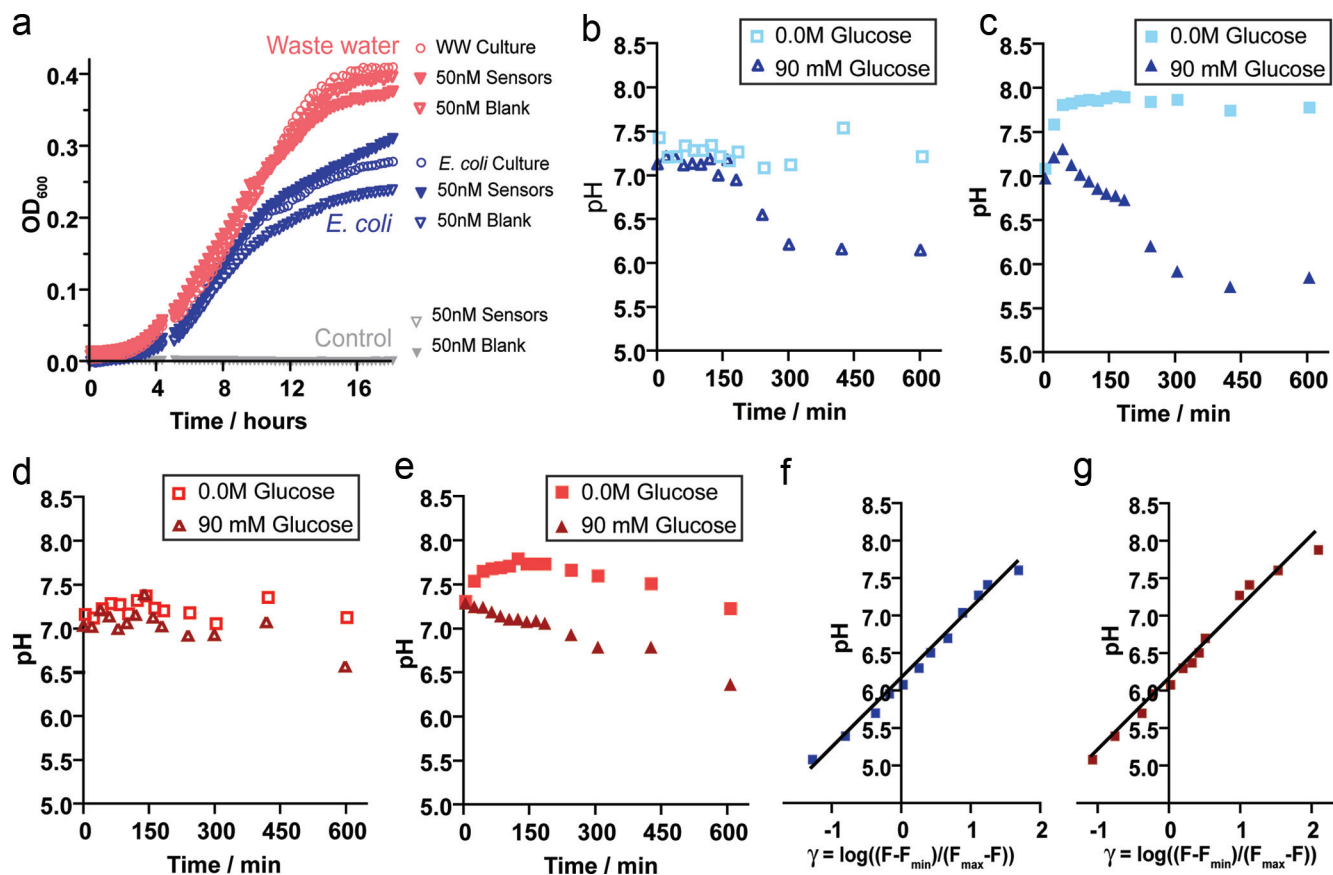


FIG. 2. C dot sensor biocompatibility, solution pH measurements, and calibrations. (a) OD at 600 nm of *E. coli* PHL628 (middle curves, shown in blue), a mixed wastewater culture (top curves, shown in red), and sterile controls (along the x axis, black) versus time under normal growth conditions (\circ) and in the presence of 50 nM C dot sensors (\blacktriangledown) or 50 nM pure silica nanoparticles of the same size (∇). (b to e) pH versus time after glucose introduction as measured by silica nanoparticle sensors (b and d) and a pH meter (c and e) in planktonic *E. coli* (b and c) and wastewater culture (d and e) suspensions. Squares and triangles indicate glucose additions of 0 and 90 mM, respectively. (f and g) pH calibration graphs for *E. coli* biofilm imaging (f) ($r^2 = 0.99$) and wastewater mixed-culture biofilm imaging (g) ($r^2 = 0.99$) based on pixelwise image analysis of confocal microscopy images of particles suspended in pH-calibrated solutions.

during and after the washing. However, the possibility that the particles were not all completely immobilized was not considered an issue of concern because, as mentioned earlier, each C dot sensor has its own internal reference. This implies that each measurement is an individual determination of the pH in the surroundings of the particle, regardless of the state of the attachment.

The growth curves presented in Fig. 2a reveal that bacterial growth is not affected by the introduction of 10 nm C dot sensor particles or dye-free silica nanoparticles of similar size. The OD reached after 18 h of growth was, on average, 0.33 for the *E. coli* PHL628 culture and 0.46 for the wastewater culture, with minimal effect of particle type (Fig. 2a) or concentration (see Fig. S2 in the supplemental material). The OD of sterile controls remained constant at approximately 0.0.

pH measurement in suspended cultures. The pH profiles after glucose addition to *E. coli* PHL628 cultures and to mixed community wastewater cultures are shown in Fig. 2 panels b and c and panels d and e, respectively. The pH was tracked both with C dots (Fig. 2b and d) and with a pH meter (Fig. 2c and e). For these samples, the trends in pH as measured over time using C dot sensors and a pH meter are comparable.

Naturally, one would expect a pH electrode to provide measurements that are less noisy but also with less spatial localization. Conversely, when using C dots for biofilm pH measurements, the values are averaged over much smaller volumes, such that each pixel has a specific spatial location and is assigned a pH value. Hence, anywhere a fluorescent bead may be present within a biofilm, i.e., attached to a cell or to extracellular polysaccharide or floating inside a pore, the pH corresponding to that location may be quantified. This explains how, within a biofilm, pH microenvironments may be observed with this technique. These results validate our claim that C dots may be used for real-time tracking of pH in bacterial environments.

Figure 2b and c show that the pH of a suspended *E. coli* PHL628 culture after glucose addition dropped from 7.0 to nearly 5.5 over ~ 400 min. Over the course of the experiment, the pH did not return to neutral values. We do not believe this acidification to be the result of fermentation because the cultures were stirred continuously to maintain aerobic conditions.

As shown in Fig. 2d and e, the decrease in pH in the mixed culture exposed to 90 mM glucose over the course of the experiment was minimal. This difference, relative to the behavior of the *E. coli* culture, is reasonable given that glucose is

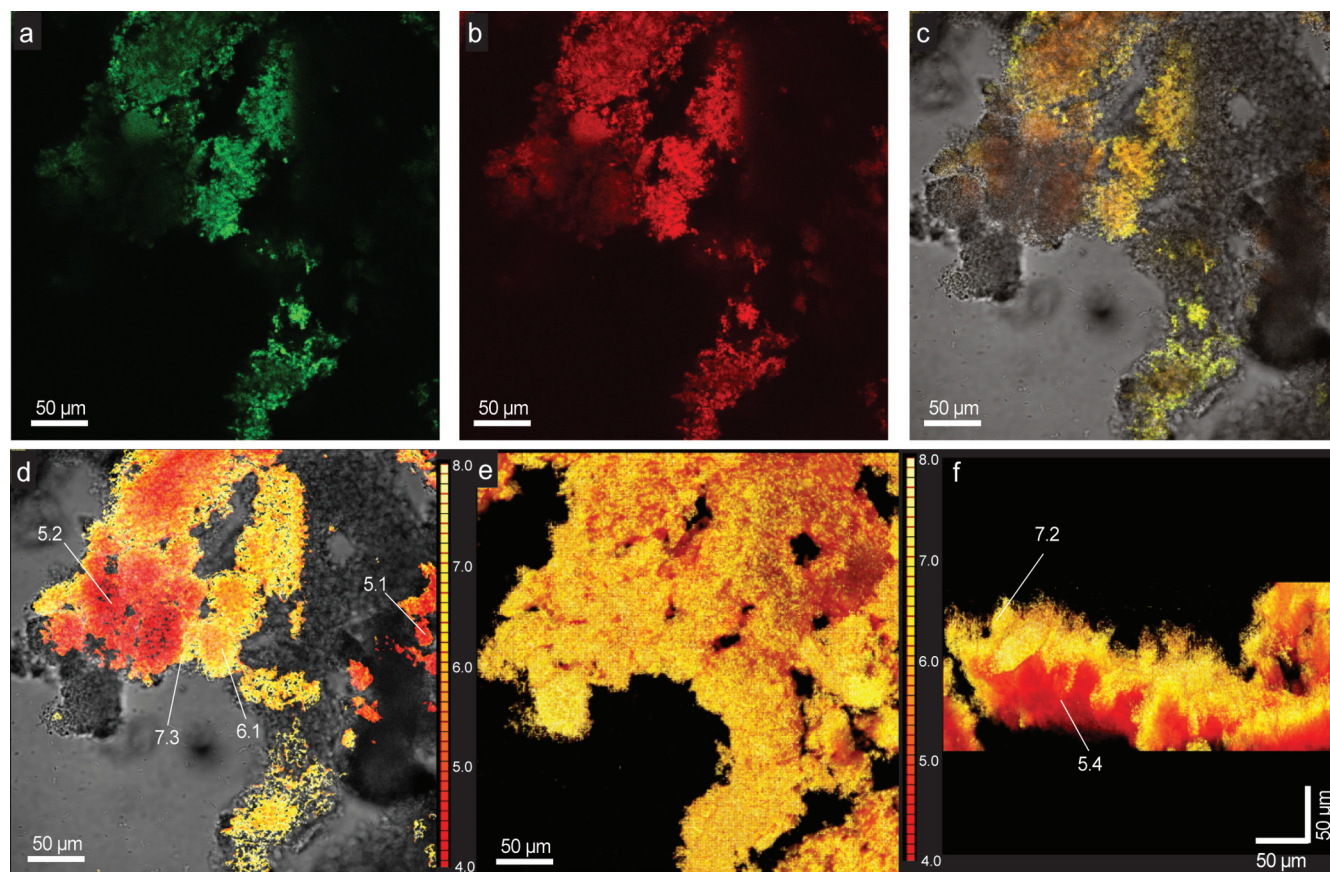


FIG. 3. *E. coli* confocal and tomographic pH imaging. (a) Green and (b) red channel confocal images of a typical live, hydrated *E. coli* PHL628 biofilm at a focal plane 90 μm from the substratum. (c) Sensor and reference images superimposed on a bright-field image of the biofilm, showing the colocalization of the particles in the film. The pH was analyzed ratiometrically based on the sensor and reference images and is expressed as a false spectrum (red-yellow) in panel d overlaid on the bright-field image, with the pH scale shown at the right. (e) Top-down and (f) side volumetric projections (smooth opacity, OsiriX) of the reconstructed biofilm pH map show the local variation in pH from the neutral outside surface of the film to the acidic core (scales in panels e and f). pH values are shown at a few sites in panels d and f to show the gradients.

the primary energy source for this enteric bacterium, which constitutively expresses the necessary enzymes for glucose metabolism (40). Therefore, in *E. coli*, catabolism can begin immediately upon glucose exposure, leading to a pH drop as metabolites accumulate in solution. The mixed wastewater culture, however, includes a wide variety of microorganisms, of which some are unable to consume glucose and others must undergo an induction process to metabolize glucose, resulting in a pH drop that is both of a smaller magnitude and delayed.

Functional 3D tomographic imaging. In Fig. 2f and g, we show the image-based pH calibration graphs for the (panel f) *E. coli* PHL628 biofilm ($r^2 = 0.99$) and (panel g) wastewater biofilm ($r^2 = 0.99$) image settings as calculated by the modified Henderson-Hasselbalch equation described in Materials and Methods, where $F_i = I_{\text{FITC}}/I_{\text{Cy5}}$ and F_{min} and F_{max} are the extreme values of F_i at low and high pHs, respectively. F_{min} , F_{max} , and F_i were calculated by pixelwise analysis of confocal microscopy images of C dot sensors suspended in calibration buffers of various pHs as described in Materials and Methods. Based on these calibration curves, we were able to accurately determine pHs ranging from 5.0 to 8.0, which covers the physiological range of this system. The two bacterial systems were analyzed on separate occasions and thus were analyzed based

on different calibration curves to correct for differences in 488- and 633-nm laser intensity, filter settings for optimal imaging, and solution conditions (Fig. 2f and g).

Figure 3a and b show, respectively, the green (sensor dye) channel and the red (reference dye) channel confocal images of a typical live, hydrated *E. coli* PHL628 biofilm at a focal plane 90 μm from the attachment substratum. Figure 3c depicts the sensor and reference images merged with a bright-field image of the biofilm, demonstrating the incorporation of the particles within the film. The greater depth of field of the bright-field image shows the structure of the film above and below the confocal image plane, which accounts for the apparent mismatch of the fluorescence and bright-field images. Vertical scanning of the sample results in registry of particle fluorescence with the bright-field images of the biofilm over the full z range of imaging (top maximum intensity projection, Fig. 3e).

The pH was analyzed ratiometrically based on the sensor and reference images and is expressed in pseudocolor (red-yellow) in Fig. 3d overlaid on the bright-field image. The pH scale is shown at the right. Specifically, the pH within the core of the biofilm is low (red) and increases (orange/yellow) toward the periphery of the film, potentially due to low rates of

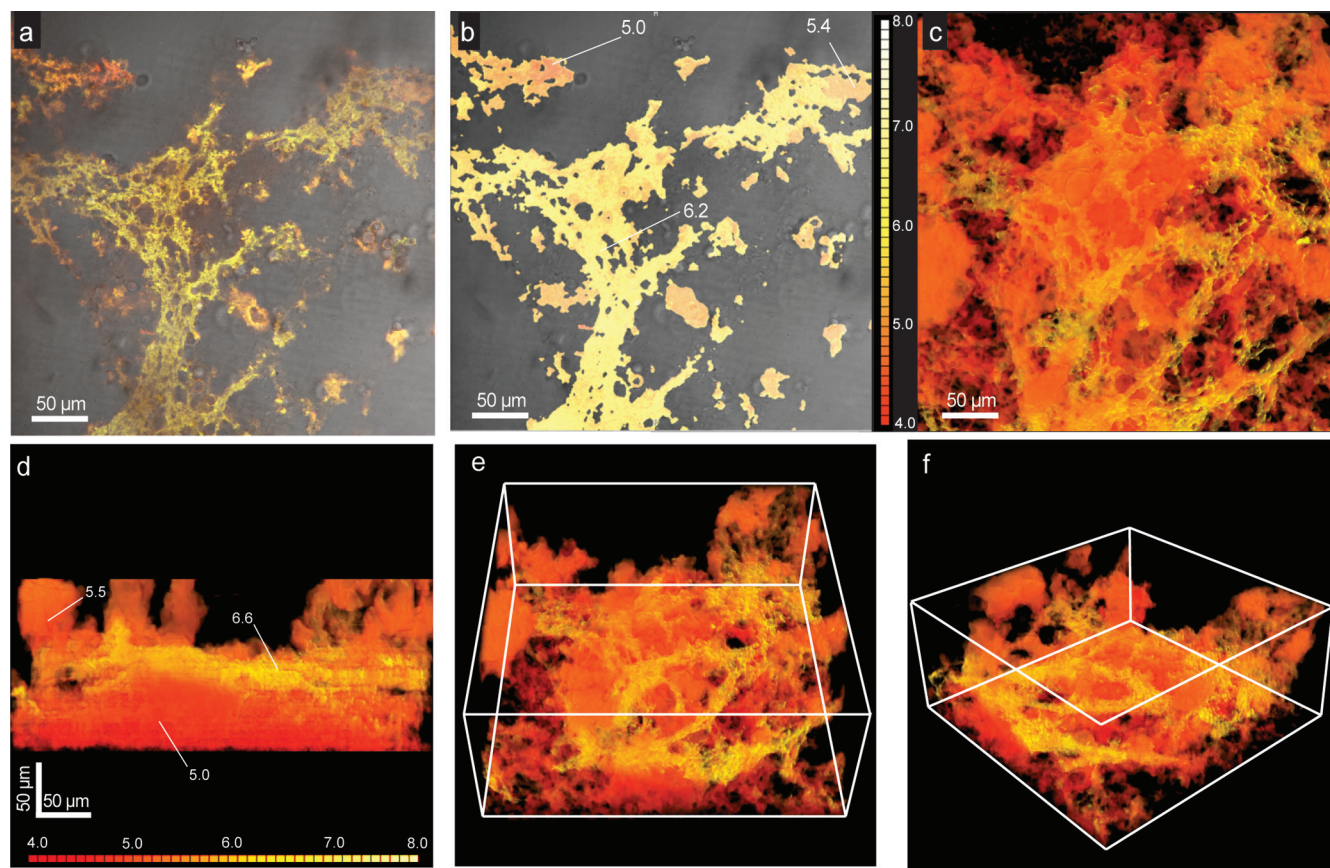


FIG. 4. Mixed-culture confocal and tomographic pH images. (a) Sensor and reference confocal images of a live, hydrated wastewater biofilm at a focal plane $77\ \mu\text{m}$ from the substratum superimposed on a bright-field image of the biofilm showing the colocalization of the particles in the film. The pH was analyzed ratiometrically based on the sensor and reference images and is expressed as a false spectrum (red-yellow) in panel b and overlaid on the bright-field image with the pH scale shown at the right. Top-down (c) and side (d) maximum-intensity projections of the biofilm. (e and f) Off-axis maximum-intensity projections of the fully reconstructed biofilm pH map (500 by 500 by $160\ \mu\text{m}$) showing the considerable heterogeneity that exists within the mixed-culture film, where a weblike neutral environment exists within the acidic film with tower structures surrounding and penetrating it.

diffusion of acidic metabolites into solution or the accumulation of fermentation products in oxygen-limited portions of the biofilm. This region of the biofilm was imaged from the attachment substratum up through a depth of $160\ \mu\text{m}$ in $1\text{-}\mu\text{m}$ steps and volumetrically reconstructed to show the biofilm morphology, as well as the pH gradients and microenvironments in the x , y , and z directions. Top and side maximum projections are presented in Fig. 3e and f, respectively. The vertical gradient from low pH deep in the film to more neutral pH at the upper surface observed in the side view (Fig. 3f) correlates well with the in-plane gradients shown in Fig. 3d. For a “fly-through” movie of the full tomographic reconstruction, see Video S1 in the supplemental material.

It is worth pointing out that Fig. 3c and 4a show the merged green and red channel images over the bright-field image as viewed on the microscope. Because, when using C dots, the intensity of the red channel is constant and that of the green signal increases with pH, the images locally appear red, yellow, and green, depending on the local intensity of sensor and reference emission. While these overlaid images provide a qualitative assessment of pH, the on-scope calibrations (Fig. 2f and g) convert the green/red intensity ratio to pH for each

pixel. These data are represented as ratiometric pH maps (Fig. 3d to f, 4b to f, 5a to f, and 6b and c) which use a false spectrum to represent the local pH, from red to yellow, as shown in the scale appended to each image or series. These false-color pH maps were generated with Osirix image processing software by using a color lookup table.

Figure 4a and b depict the overlay and ratiometric pH images of a mixed-culture biofilm $77\ \mu\text{m}$ from the substratum. The pH is more heterogeneous throughout this mixed culture than the axenic one, both horizontally and vertically, as revealed by the variation in top and side maximum-intensity projections in Fig. 3e and f and 4c and d. Figure 4e and f show the distinct pH microenvironments in the 3D pH image of the mixed-culture film by presenting projections of the full tomographic reconstruction (500 by 500 by $160\ \mu\text{m}$). For the corresponding fly-through video, see Video S2 in the supplemental material. Based on the morphological and chemical differences between microenvironments, it is likely that bacteria from different functional groups are coexisting and generating different metabolic by-products.

Investigating specific regions of interest by zooming into the full tomographic reconstructions and providing various views

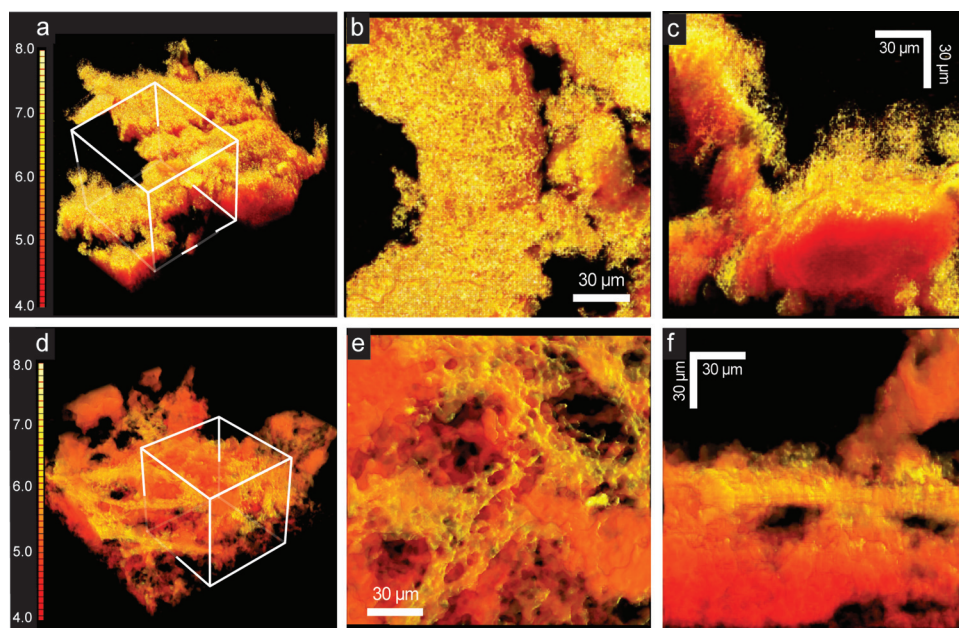


FIG. 5. Magnified views of regions of interest in *E. coli* and mixed-culture biofilms. (a) Off-axis maximum-intensity projection of the reconstructed *E. coli* PHL628 biofilm and pH map scale at the left (pHs 4.0 to 8.0, red-yellow). For panels a and d, a region of interest was defined by the white cube (160 by 160 by 160 μm). Panels b and c are top and side views of the region of interest defined by the white cube in panel a, showing the pH heterogeneities, as well as the local structure, of the biofilm. (d) Off-axis volumetric (smooth table) projection of the reconstructed wastewater mixed-culture biofilm and pH map scale at the left (pHs 4.0 to 8.0, red-yellow). (e and f) Top and side views of the cube shown in panel d showing the pH heterogeneities, as well as the local structure, of the biofilm, including voids, channels, and a tower.

of the *E. coli* and mixed-culture biofilms (Fig. 5) demonstrates the power of nanoparticle sensor-enabled 3D functional imaging. Figure 5a to c show in detail the low-to-neutral pH gradient formed from the core of the biofilm to the periphery, as well as the fine structure with channels and voids of the *E. coli* film. Figure 5d to f show the voids formed by the interpenetration of the low-pH film components and the fibrous neutral regions, as well as the different growth habits of the two, including a mushroom-like protrusion in the mixed-culture biofilm.

Figure 6a depicts the average pH versus time following a glucose injection (90 mM) for *E. coli* PHL628 (red) and waste-

water mixed culture (blue) biofilms. Figure 6b and c show the corresponding confocal ratiometric pH images at $t = 0$ and 90 min, respectively, after glucose addition to the *E. coli* PHL628 biofilm at a focal plane 60 μm from the attachment substratum (for further images, see the supplemental material).

The *E. coli* biofilm pH drops sharply from 6.3 to 5.2 in the first 30 min and then remains constant for the remainder of the experiment. The wastewater biofilm follows a similar trend, though the magnitude of the pH change is smaller (plateau value of 5.6 at 90 min; see the images in the supplemental material). This result is similar to the behavior observed in the

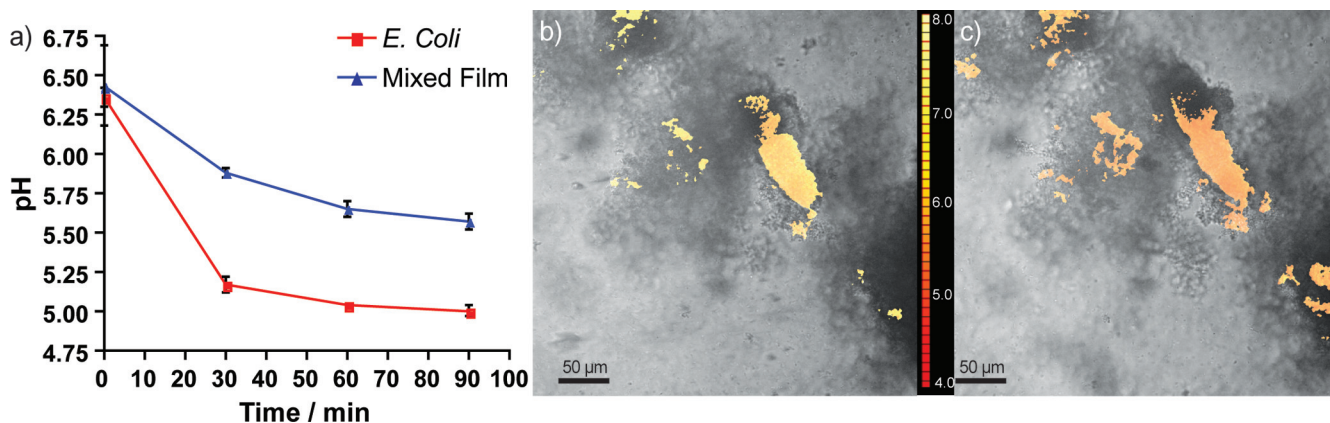


FIG. 6. Time-resolved in situ pH measurements in biofilms. (a) Average pH versus time postinjection of 90 mM glucose into biofilms of *E. coli* PHL628 (in red, mean \pm standard deviation, $n = 3$) and mixed wastewater culture (in blue, mean \pm standard deviation, $n = 6$). Values are significantly different from $t = 30$ min onward (one-tailed Mann-Whitney U test, $P = 0.011$). (b and c) Imaging of C dots within an *E. coli* PHL628 biofilm corresponding to the initial (b) and final (c) time points of the graph shown in panel a (the color scale corresponds to pHs of 4 to 8).

suspended cultures, though the kinetics are much faster in the biofilms. The increased rate of pH change in the biofilm is most likely due to the fact that diffusion is hindered in the biofilm compared to that in the stirred suspensions, allowing acidic metabolites to accumulate in the biofilm and change the local pH more quickly.

All of the biofilm imaging experiments were performed without shaking or perfusion in order to maintain a stable field of view over the course of the experiment. Therefore, the rate of oxygen diffusion was low and anoxic zones may have developed within the biofilms. So, in contrast to the planktonic cultures (Fig. 2b to e), it is possible that the drop in pH observed in the biofilms (Fig. 6a) is the combined result of limited diffusion and different metabolic processes, i.e., aerobic and anaerobic respiration and fermentation. In the case of the wastewater culture biofilm, the presence of glucose fermenters (such as other species of enteric bacteria, *Clostridium*, *Lactobacillus*, and even yeasts) might also explain the presence of the low-pH microenvironments.

DISCUSSION

In nanobiotechnology, tools of nanotechnology are used to study biology and in particular to further the goals of biotechnology. Over the past 2 decades, fueled by the discovery of fluorescent semiconductor nanocrystals, an explosion has taken place in the development of fluorescent nanoparticles and nanoparticle systems for imaging, sensing, and diagnostic purposes (35, 39). Concurrently, microscale heterogeneities in biofilms, in particular, sucrose-induced pH gradients in dental caries, have been the subject of much research (13, 21, 27, 28, 34, 37, 42, 45–47, 55). However, despite recent advances, our present understanding of the complex processes that occur in biofilms is incomplete. The presence of biofilms at the solid-water interface in virtually all systems allows them to impact the quality of water in the environment, regulate the behavior and fate of pollutants, enhance the resistance of infections to treatment, and, in short, have an effect on all ecosystems and the organisms that inhabit them (41). Concomitant with increasing recognition of the importance of biofilms is the need for better investigational tools. Development and execution of in situ monitoring and characterization of biofilms are expected to be particularly powerful to address present and future needs. Toward this end, the research presented here demonstrates, for the first time, the use of ratiometric fluorescent silica nanoparticle sensors as tools for high-resolution 3D and time domain functional fluorescence imaging of pH gradients in microbial biofilms. These nanoparticle sensors provide a minimally invasive route to quantitative chemical imaging with resolution limited only by the microscopy system used.

For nanoparticle sensor-based functional imaging of biofilms to work, the nanoparticle probes must intimately mix with and stay in the extracellular matrix of the biofilm. Interestingly, by performing experiments with 70-, 30-, and 10-nm-diameter silica particles, we found that only the smallest bare C dot sensors provided the desired effective and homogeneous staining. There are several effects which, by themselves or in combination, could explain these observations. Gels of polysaccharides and fibrous proteins fill the intercellular spaces of biofilms. First, fluid gaps between these elements of the extra-

cellular matrix could simply be too small for the bigger particles to penetrate. Second, it is expected that mixing between nanoparticles and polymer matrices is size dependent for entropic reasons. In fact, such entropic size dependencies have been theoretically predicted and experimentally observed (32, 52, 56). For mixing to occur, polymer chains must wrap around the nanoparticles, a process which becomes more entropically unfavorable as the particle size increases relative to the polymer size. Because polymer dimensions scale with only the square root of the number of units constituting them (ideal case) (10), particle size quickly outgrows chain size. Plugging in relevant values for extracellular matrix polymer sizes (data not shown) suggests that it is not unreasonable to expect the critical particle size for demixing to be between 10 and 30 nm. Third, the electrostatic repulsion between the negatively charged particle surfaces and biofilm extracellular matrix could cause a similar size-dependent effect. The electrostatic repulsion energy for particles of uniform surface charge scales approximately with the surface area of the particles (20), such that 70-nm-diameter particles would experience an ~50-fold stronger repulsion than 10-nm-diameter particles, making their inclusion in the biofilm much less favorable. While repulsive electrostatic effects will be partially screened by the ions in solution (e.g., 0.05 M NaCl in LB medium), they may still affect the behavior at small length scales. Irrespective of which of these effects dominates the behavior, particle size becomes a critical design criterion for nanoparticle probes for biofilm interrogation.

The dyes in the C dot sensors are shielded by the silica matrix from interactions with extracellular matrix components that can bias the results, which simultaneously renders the particles biocompatible for use in both prokaryotic and higher biological systems with minimal toxicity. The enhanced photostability of the silica-encapsulated dye molecules also facilitates high-resolution x - y - z and x - y time-space measurements without compromising sensitivity. Although the long-wavelength photons used in multiphoton imaging give greater penetration depth than single-photon imaging, for this work a dual-excitation, single-photon system was chosen to provide a large spectral separation between sensor and reference emissions. Several recent reviews further elaborate on the relative merits of single and multiphoton imaging techniques (19, 57).

The sensor-reference dye combination chosen for this work is well suited to the pH values in living biofilms, but other combinations can be synthesized to study environments with more extreme pH gradients, such as microbial mats (53), insect midguts (3), and river sediments exposed to acid mine drainage (1). Substituting a fluorophore with a more acidic or basic pK_a such as Oregon Green 514 or carboxynaphthofluorescein (4.8 and 7.6, respectively [18]) for fluorescein allows the linear range of the particles to be tailored. Moreover, by changing to other dyes, it is possible to quantitatively measure other variables of interest, such as redox potential, oxygen status, or the concentration of ions such as Ca^{2+} and Mg^{2+} , without significantly altering the particle architecture. Such nanoparticle probes, if designed appropriately, should provide powerful tools for future in situ monitoring and characterization of complex biofilms.

Future work will explore the potential correlations between heterogeneities in pH (i.e., in mixed-culture biofilms) and the

bacterial species present at those locations. This line of research can be carried out by fluorescence in situ hybridization performed on biofilms colabeled with pH-sensing C dots. This objective might also be pursued by staining of extracellular products with fluorescent lectins specific for the polysaccharides that are produced by the particular microorganisms which are being tested, followed by concurrent imaging of the lectins and the sensor particles. The latter approach, although indirect, may provide an interesting and so-far-unexplored perspective.

ACKNOWLEDGMENTS

We appreciate the assistance of Carol Bayles and the Microscopy and Imaging Facility of the Cornell Biotechnology Research Center.

Gabriela Hidalgo was funded through a CONACYT graduate fellowship. This work was supported in part by NSF grant EAR-0311767. Andrew Burns was supported by the Cornell Nanobiotechnology Center (NBTC), an STC center of the NSF, under agreement ECS-9876771.

U.W. has a financial role in a start-up company (Hybrid Silica Technologies) in the field of fluorescent nanoparticle development.

REFERENCES

- Blöthe, M., D. M. Akob, J. E. Kostka, K. Goschel, H. L. Drake, and K. Kusel. 2008. pH gradient-induced heterogeneity of Fe(III)-reducing microorganisms in coal mining-associated lake sediments. *Appl. Environ. Microbiol.* **74**:1019–1029.
- Botvinick, E. L., and J. V. Shah. 2007. Laser-based measurements in cell biology. *Methods Cell Biol.* **82**:81–109.
- Brune, A., D. Emerson, and J. A. Breznak. 1995. The termite gut microflora as an oxygen sink: microelectrode determination of oxygen and pH gradients in guts of lower and higher termites. *Appl. Environ. Microbiol.* **61**:2681–2687.
- Burns, A., H. Ow, and U. Wiesner. 2006. Fluorescent core-shell silica nanoparticles: towards “Lab on a Particle” architectures for nanobiotechnology. *Chem. Soc. Rev.* **35**:1028–1042.
- Burns, A., P. Sengupta, T. Zedayko, B. Baird, and U. Wiesner. 2006. Core-shell fluorescent silica nanoparticles for chemical sensing: towards single-particle laboratories. *Small* **2**:723–726.
- Chang, C. W., D. Sud, and M. A. Mycek. 2007. Fluorescence lifetime imaging microscopy. *Methods Cell Biol.* **81**:495–524.
- Choi, J. H., A. A. Burns, R. M. Williams, Z. X. Zhou, A. Flesken-Nikitin, W. R. Zipfel, U. Wiesner, and A. Y. Nikitin. 2007. Core-shell silica nanoparticles as fluorescent labels for nanomedicine. *J. Biomed. Opt.* **12**:064007. doi:10.1117/1.2823149.
- Clark, H. A., M. Hoyer, M. A. Philbert, and R. Kopelman. 1999. Optical nanosensors for chemical analysis inside single living cells. 1. Fabrication, characterization, and methods for intracellular delivery of PEBBLE sensors. *Anal. Chem.* **71**:4831–4836.
- de Beer, P., P. Stoodley, F. Roe, and Z. Lewandowski. 1994. Effects of biofilm structures on oxygen distribution and mass transport. *Biotechnol. Bioeng.* **43**:1131–1138.
- De Gennes, P.-G. 1979. Scaling concepts in polymer physics. Cornell University Press, Ithaca, NY.
- Dethlefsen, L., M. McFall-Ngai, and D. A. Relman. 2007. An ecological and evolutionary perspective on human-microbe mutualism and disease. *Nature* **449**:811–818.
- Donlan, R. M. 2002. Biofilms: microbial life on surfaces. *Emerg. Infect. Dis.* **8**:881–890.
- Ferris, M. J., T. S. Magnuson, J. A. Fagg, R. Thar, M. Kühn, K. B. Sheehan, and J. M. Henson. 2003. Microbially mediated sulphide production in a thermal, acidic algal mat community in Yellowstone National Park. *Environ. Microbiol.* **5**:954–960.
- Giesecke, A., S. Tarre, M. Green, and D. de Beer. 2006. Nitrification in a biofilm at low pH values: role of in situ microenvironments and acid tolerance. *Appl. Environ. Microbiol.* **72**:4283–4292.
- Gilbert, P., T. Maira-Litran, A. J. McBain, A. H. Rickard, and F. W. Whyte. 2002. The physiology and collective recalcitrance of microbial biofilm communities. *Adv. Microb. Physiol.* **46**:202–256.
- Gryczynski, Z., I. Gryczynski, and J. R. Lakowicz. 2003. Fluorescence-sensing methods. *Methods Enzymol.* **360**:44–75.
- Hall-Stoodley, L., J. W. Costerton, and P. Stoodley. 2004. Bacterial biofilms: from the natural environment to infectious diseases. *Nat. Rev. Microbiol.* **2**:95–108.
- Haugland, R. P. 2007. The handbook—a guide to fluorescent probes and labeling technologies, 10th ed. Molecular Probes, Inc., Eugene, OR.
- Helmchen, F., and W. Denk. 2005. Deep tissue two-photon microscopy. *Nat. Methods* **2**:932–940.
- Hermansson, M. 1999. The DLVO theory in microbial adhesion. *Colloids Surf. B Biointerfaces* **14**:105–119.
- Hunter, K. S., Y. Wang, and P. Van Cappellen. 1998. Kinetic modeling of microbially-driven redox chemistry of subsurface environments: coupling transport, microbial metabolism and geochemistry. *J. Hydrol.* **209**:53–80.
- Hunter, R. C., and T. J. Beveridge. 2005. Application of a pH-sensitive fluorophore (C-SNARF-4) for pH microenvironment analysis in *Pseudomonas aeruginosa* biofilms. *Appl. Environ. Microbiol.* **71**:2501–2510.
- Ito, T., J. L. Nielsen, S. Okabe, Y. Watanabe, and P. H. Nielsen. 2002. Phylogenetic identification and substrate uptake patterns of sulfate-reducing bacteria inhabiting an oxic-anoxic sewer biofilm determined by combining microautoradiography and fluorescent in situ hybridization. *Appl. Environ. Microbiol.* **68**:356–364.
- Kaewpipat, K., and C. P. Grady, Jr. 2002. Microbial population dynamics in laboratory-scale activated sludge reactors. *Water Sci. Technol.* **46**:19–27.
- Kemner, K. M., S. D. Kelly, B. Lai, J. Maser, J. O’Loughlin, E., D. Sholto-Douglas, Z. Cai, M. A. Schneegurt, C. F. Kulpa, Jr., and K. H. Nealson. 2004. Elemental and redox analysis of single bacterial cells by X-ray microbeam analysis. *Science* **306**:686–687.
- Koo, Y. E. L., Y. F. Cao, R. Kopelman, S. M. Koo, M. Brasuel, and M. A. Philbert. 2004. Real-time measurements of dissolved oxygen inside live cells by organically modified silicate fluorescent nanosensors. *Anal. Chem.* **76**:2498–2505.
- Kühl, M. 2005. Optical microsensors for analysis of microbial communities. *Methods Enzymol.* **397**:166–199.
- Kühl, M., and T. Fenchel. 2000. Bio-optical characteristics and the vertical distribution of photosynthetic pigments and photosynthesis in an artificial cyanobacterial mat. *Microb. Ecol.* **40**:94–103.
- Küseler, A., V. Baelum, O. Fejerskov, and J. Heidmann. 1993. Accuracy and precision in vitro of Beetrode microelectrodes used for intraoral pH measurements. *Caries Res.* **27**:183–190.
- Lappin-Scott, H. M., and J. W. Costerton. 1989. Bacterial biofilms and surface fouling. *Biofouling* **1**:323–342.
- Larson, D. R., H. Ow, H. D. Vishwasrao, A. A. Heikal, U. Wiesner, and W. W. Webb. 2008. Silica nanoparticle architecture determines radiative properties of encapsulated fluorophores. *Chem. Mater.* **20**:2677–2684.
- Mackay, M. E., A. Tuteja, P. M. Duxbury, C. J. Hawker, B. Van Horn, Z. B. Guan, G. H. Chen, and R. S. Krishnan. 2006. General strategies for nanoparticle dispersion. *Science* **311**:1740–1743.
- Marquis, R. E. 1995. Oxygen metabolism, oxidative stress and acid-base physiology of dental plaque biofilms. *J. Ind. Microbiol.* **15**:198–207.
- Marsh, P. D., and D. J. Bradshaw. 1995. Dental plaque as a biofilm. *J. Ind. Microbiol.* **15**:169–175.
- Michalet, X., F. F. Pinaud, L. A. Bentolila, J. M. Tsay, S. Doose, J. J. Li, G. Sundaresan, A. M. Wu, S. S. Gambhir, and S. Weiss. 2005. Quantum dots for live cells, in vivo imaging, and diagnostics. *Science* **307**:538–544.
- Okabe, S., T. Itoh, H. Satoh, and Y. Watanabe. 1999. Analyses of spatial distributions of sulfate-reducing bacteria and their activity in aerobic wastewater biofilms. *Appl. Environ. Microbiol.* **65**:5107–5116.
- Okabe, S., H. Satoh, and Y. Watanabe. 1999. In situ analysis of nitrifying biofilms as determined by in situ hybridization and the use of microelectrodes. *Appl. Environ. Microbiol.* **65**:3182–3191.
- Palmer, R. J., Jr., and C. Sternberg. 1999. Modern microscopy in biofilm research: confocal microscopy and other approaches. *Curr. Opin. Biotechnol.* **10**:263–268.
- Piao, Y., A. Burns, J. Kim, U. Wiesner, and T. Hyeon. 2008. Designed fabrication of silica-based nanostructured particle systems for nanomedicine applications. *Adv. Funct. Mater.* **18**:3745–3758.
- Plumbridge, J. 1998. Control of the expression of the manXYZ operon in *Escherichia coli*: Mlc is a negative regulator of the mannose PTS. *Mol. Microbiol.* **27**:369–380.
- Potera, C. 1996. Biofilms invade microbiology. *Science* **273**:1795–1797.
- Ramsing, N. B., M. Kühn, and B. B. Jørgensen. 1993. Distribution of sulfate-reducing bacteria, O₂, and H₂S in photosynthetic biofilms determined by oligonucleotide probes and microelectrodes. *Appl. Environ. Microbiol.* **59**:3840–3849.
- Roeselers, G., M. C. M. van Loosdrecht, and G. Muyzer. 2008. Phototrophic biofilms and their potential applications. *J. Appl. Phycol.* **20**:227–235.
- Rosset, A., L. Spadola, and O. Ratib. 2004. OsiriX: an open-source software for navigating in multidimensional DICOM images. *J. Digital Imaging* **17**:205–216.
- Sissons, C. 1998. Plaque, plaque model systems and pH. *N. Z. Dent. J.* **94**:56–60.
- Sissons, C. H., T. W. Cutress, G. Faulds, and L. Wong. 1992. pH responses to sucrose and the formation of pH gradients in thick ‘artificial mouth’ microcosm plaques. *Arch. Oral Biol.* **37**:913–922.
- Sissons, C. H., L. Wong, E. M. Hancock, and T. W. Cutress. 1994. pH gradients induced by urea metabolism in ‘artificial mouth’ microcosm plaques. *Arch. Oral Biol.* **39**:507–511.

48. Stewart, P. S., and M. J. Franklin. 2008. Physiological heterogeneity in biofilms. *Nat. Rev. Microbiol.* **6**:199–210.
49. Stief, P., and G. Eller. 2006. The gut microenvironment of sediment-dwelling *Chironomus plumosus* larvae as characterised with O₂, pH, and redox microsensors. *J. Comp. Physiol. B* **176**:673–683.
50. Stöber, W., A. Fink, and E. Bohn. 1968. Controlled growth of monodisperse silica spheres in micron size range. *J. Colloid Interface Sci.* **26**:62–69.
51. Stoodley, P., K. Sauer, D. G. Davies, and J. W. Costerton. 2002. Biofilms as complex differentiated communities. *Annu. Rev. Microbiol.* **56**:187–209.
52. Thompson, R. B., V. V. Ginzburg, M. W. Matsen, and A. C. Balazs. 2001. Predicting the mesophases of copolymer-nanoparticle composites. *Science* **292**:2469–2472.
53. Vasconcelos, C., R. Warthmann, J. A. McKenzie, P. T. Visscher, A. G. Bittermann, and Y. van Lith. 2006. Lithifying microbial mats in Lagoa Vermelha, Brazil: modern Precambrian relics? *Sediment. Geol.* **185**:175–183.
54. Vidal, O., R. Longin, C. Prigent-Combaret, C. Dorel, M. Hooreman, and P. Lejeune. 1998. Isolation of an *Escherichia coli* K-12 mutant strain able to form biofilms on inert surfaces: involvement of a new *ompR* allele that increases curli expression. *J. Bacteriol.* **180**:2442–2449.
55. Vroom, J. M., K. J. De Graw, H. C. Gerritsen, D. J. Bradshaw, P. D. Marsh, K. G. Watson, J. J. Birmingham, and C. Allison. 1999. Depth penetration and detection of pH gradients in biofilms by two-photon excitation microscopy. *Appl. Environ. Microbiol.* **65**:3502–3511.
56. Warren, S. C., F. J. Disalvo, and U. Wiesner. 2007. Nanoparticle-tuned assembly and disassembly of mesostructured silica hybrids. *Nat. Mater.* **6**:156–161.
57. Williams, R. M., D. W. Piston, and W. W. Webb. 1994. 2-photon molecular-excitation provides intrinsic 3-dimensional resolution for laser-based microscopy and microphotochemistry. *FASEB J.* **8**:804–813.
58. Xi, C., D. Marks, S. Schlachter, W. Luo, and S. A. Boppart. 2006. High-resolution three-dimensional imaging of biofilm development using optical coherence tomography. *J. Biomed. Opt.* **11**:34001.